Estuarine, Coastal and Shelf Science 275 (2022) 107995

Contents lists available at ScienceDirect

Estuarine, Coastal and Shelf Science

journal homepage: www.elsevier.com/locate/ecss

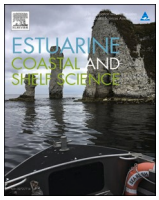

A comprehensive study of the river plume in a microtidal setting

Agnese Baldoni [a,*], Eleonora Perugini [b], Pierluigi Penna [c], Luca Parlagreco [d], Maurizio Brocchini [a]

[a] Department of Civil Engineering and Architecture (DICEA), Università Politecnica delle Marche, Ancona, Italy
[b] Department of Civil and Environmental Engineering (CEE), University of Strathclyde, Glasgow, United Kingdom
[c] National Research Council – Institute of Marine Biological Resources and Biotechnologies CNR IRBIM, Ancona, Italy
[d] Italian Institute for Environmental Protection and Research (ISPRA), Rome, Italy

ARTICLE INFO

Keywords:
River plume
Estuary
Microtidal environment
Large-scale PTV
Numerical modelling

ABSTRACT

On the basis of observations and modelling of the plume generated by the Misa River (AN, Italy), we performed a comprehensive study, which integrated different sources of information (field data, numerical simulations, etc.), of the generation and transport mechanisms of river plumes flowing into microtidal environments. First, we analysed images simultaneously acquired by both two shore-based stations and satellite to determine plume fronts and extensions. Then, we correlated such information with the estuarine forcing to recognize the plume generation and transport mechanisms. Being real-life events influenced by a combination of factors, we run numerical simulations to separately study each force and its influence on the plume evolution. We also performed simulations of two real-life cases, to compare the modelled and observed results. We identified the river discharge and the wind as the main generation and transport mechanisms, respectively. Moreover, waves could stir, suspend, and drag plume sediments, even if results showed that a river discharge associated with a return period smaller than 1 year produced a plume denser than 5-year return period waves. The transport mechanisms were responsible for the alongshore extension of the plume. The tide, even if secondarily, affected the plume evolution, depending on its phase shift to the river discharge peak. Particle Tracking Velocimetry from videos acquired by a shore-based station provided the surface velocity field in the final river stretch. This and the contributions by wind and waves were correlated with the plume extension through a power law.

1. Introduction

When a river discharge inflows to sea, it forms a buoyant plume composed of suspended and dissolved constituents that mix into sea water. Understanding of the structure, dynamics and evolution of river plumes is fundamental to comprehend the land-ocean exchanges. Plumes are classified in "large-scale" or "small-scale", respectively when large-scale rotational processes dominate over inertial processes or vice versa (Garvine, 1995). Another division of plumes in "surface-advected" and "bottom-advected" was done by Yankovsky and Chapman (1997), who distinguished between relatively shallow plumes affected by surface dynamics and plumes extending to the bottom, whose offshore extent and velocity structure are dictated by bottom Ekman dynamics and thermal wind balance. The formation and spreading of river plumes are governed by both "intrinsic characteristics", such as local latitude, topography, morphology, and sediment characteristics, and "external forcing", including river discharge, local wind, tide, coastal circulation and waves (Osadchiev and Zavialov, 2019).

While considerable attention was paid to large and medium-size systems (a. o., Yankovsky and Chapman, 1997; Fong and Geyer, 2001; Liu et al., 2009), few studies focused on small river plumes even if they contributed to 40% influx of suspended sediment to the ocean (a.o., Milliman and Syvitski, 1992; Bourrin et al., 2008; Lebedev et al., 2020). Buoyant plumes originated from small river systems have small spatial scales and, therefore, small residence time of freshened water, equal to hours and days, because of the relatively low volume of river discharge and its intense mixing with ambient sea. Osadchiev and Sedakov (2019) showed that the spreading pattern of small river plumes are different from those typical for large and medium-size rivers and largely influenced by the wind forcing. The concentration of wind stress in a shallow freshened surface layer causes higher motion velocity and more quick response of the plume dynamics to variability of wind forcing (Ostrander et al., 2008; Warrick et al., 2007). It results in wind-driven dynamics of small plumes, which is characterized by very energetic short-temporal

* Corresponding author.
E-mail address: a.baldoni@pm.univpm.it (A. Baldoni).

https://doi.org/10.1016/j.ecss.2022.107995
Received 31 January 2022; Received in revised form 5 July 2022; Accepted 15 July 2022
Available online 30 July 2022

variability of their positions, shapes, and areas (Osadchiev and Sedakov, 2019; Osadchiev et al., 2020).

Winds are dominant forcing driving the plume variability also in microtidal environments, where the tidal effects are negligible. Kombiadou and Krestenitis (2012) observed that the pathways of sediment flowing into the Thermaikos gulf (north Aegean Sea) were mainly controlled by winds and the predominant surface circulation. Other factors that influence the plume variability in microtidal sites are the site topography, the bottom slope and the river discharge (Mestres et al., 2007), found to be linearly correlated with the plume area (Lebedev et al., 2020).

In contrast, in macro and mesotidal environments, largely studied in literature, tides strongly affect the mixing and the water column stability and, therefore, the horizontal movement and spreading of plumes (a.o., Simpson et al., 1993; de Boer et al., 2009; Lee and Liu, 2013).

Finally, Rodriguez et al. (2018) showed that waves, interacting with the river current, significantly alter the plume structure. Thus, the fate of suspended sediment transported by plumes is related to the ratio of the wave-to-outflow momentum fluxes (Kastner et al., 2019; Zarzuelo et al., 2021), which in turn is influenced by the bathymetry, the tide and the phase between the river discharge and high water (Ruiz-Reina and López-Ruiz, 2021). To the authors' knowledge, the role of waves in resuspending riverbed sediment, generating a plume, has found little space in the literature.

The present study aims at characterizing, on the basis of observations and modelling of dynamics evolving at one specific but representative river, the mechanisms responsible for the formation and evolution of small-discharge river plumes in a microtidal environment using an integrated approach. The first step consisted in detecting plume occurrences and assessing plume offshore extensions through the analysis of images from video-monitoring stations and satellite. While satellite imagery allows the monitoring of river plumes behaviour over large distances (Soosaar et al., 2016), they have a limited temporal resolution and fail to provide data when cloud cover is present, commonly after a rainfall. Instead, video and images recorded by fixed stations provide data on the hourly evolution of the plume and are, therefore, appropriate for studying small-scale plumes (Morichon et al., 2008). Their main advantages are acquisition frequency flexibility, high spatial resolution, weak climate dependency, and low cost compared with commonly used remote-sensing techniques to operationally estimate river plumes. We correlated the information obtained from the image analysis with the forces acting in the estuarine area to recognize the plume generation and transport mechanisms. However, being real-life events characterized by a combination of factors, it was complicated to define the role of each forcing in the plume evolution. Therefore, we decided to run numerical simulations to separately study the effect of single forces and verify the consistency of the results with the observations. In this perspective, we also run two simulations reproducing real-life events. Finally, we performed Particle Tracking Velocimetry (PTV) analyses to find a relationship between plume extensions and velocities, taking into account the mechanisms that have been found to influence more the plume evolution. The issues we focused on are: i) the plume local generation mechanisms, causing sediment resuspension inside the river channel, in a microtidal environment; ii) the extension of the plume and its relationship with the plume velocity; iii) the forcing affecting the plume evolution.

Section 2 describes the characteristics of the studied area and of the video-monitoring stations, including the technique used to post-process the images and extract the plume extent, and outlines all the other datasets used for the analysis. The PTV technique and the set-up of the numerical model used to simulate the plume evolution are also included in Section 2. Section 3 reports the results of field observations, numerical simulations and PTV analyses, while discussion and conclusions are given in Section 4 and Section 5, respectively.

2. Materials and methods

2.1. Field site

The study area includes the Misa River estuary (MRE hereinafter) (Senigallia, Marche, Italy, Fig. 1a) and the surrounding beach. Focus is on the stretch of beach that extends from the river jetty to around 2 km south of the MRE because: i) the main video-monitoring system used for the analysis faces toward the south and provides information on that stretch of coast in combination with a twin ISPRA station, this being a strength of the present analysis; ii) the majority of plumes observed during events (86%) bent toward the south; iii) the coast north of the harbour is protected by emerged breakwaters, limiting the impact of the plume on the beach. The coast of Senigallia, along the Adriatic Sea in central Italy, is located in a microtidal environment, with tidal range rarely exceeding 0.6 m (www.mareografico.it; Mohamed et al., 2019). The coastline has a NW–SE orientation and faces approximately 40° from the north. The submerged beach to the south of the river jetty is characterized by fine-to-medium sands with a median grain size (D_{50}) of 0.125–0.25 mm (Postacchini et al., 2017) and usually features an array of three–four shore-parallel, shallow bars within 300 m from the shoreline, in water depths between 0 and 3 m.

The wave climate along the coast of Senigallia is characterized by two main wave regimes, generated by dominant and prevailing winds blowing on the Adriatic Sea, namely, Bora and Scirocco. They are, respectively, a short-fetch strong north-easterly wind and a long-fetch south-easterly wind, blowing along the minor and major axis of the Adriatic basin. The largest waves are generated during Bora storms and approach from NNE, even though energetic Scirocco-driven waves from E are frequently observed (Fig. 2). The annual average significant wave height is of 0.43 m and the peak period is of 4.5 s. Both NNE and E waves can enter the river channel, but since the final stretch of the MR faces approximately 30° from the north, NNE waves penetrate more easily than E waves. Wind statistics and directional roses are shown in Fig. 2. The most frequent wind comes from WSW and is associated with low speeds (3–6 m/s). The most intense winds blow from NNE and W-WNW. The mean annual wind speed is 3.87 m/s.

The watershed extension of the Misa River (MR hereinafter) is 383 km^2, with discharges of about 400, 450, and 600 $m^3\ s^{-1}$ for return periods of 100, 200, and 500 years, respectively. The river discharge associated to a return period of 1 year is 150 m^3/s, while the low-water discharge is about 2.5 m^3/s. The river width is between 20 and 30 m and the water depth in the channel is less than 2.5 m.

The MR behaves as other Apennine Mountains rivers: although relatively small in size, it distributes large quantities of sediment, generated by the easy erosion of the rocks that constitute the Apennine Mountains. The suspended sediment discharge from the MR is estimated to be between $4.7{\cdot}10^8$ kg yr^{-1} and $8.4{\cdot}10^8$ kg yr^{-1} (Milliman and Syvitski, 1992; Frignani et al., 2005). The sediment grain sizes throughout the MR can range from clay to cobble. The deposition of volcanic ash, transported from the southeast by winds during the Plinian and other volcanic eruptions (Pigorini, 1968; Rolandi et al., 2008), has enhanced the cohesive nature of the sediments within the MR, by adding an abundant supply of montmorillonite clay minerals (2–5 μm in size).

Cores of the alluvial layers that underlie the town of Senigallia, collected by Favali et al. (1995), displayed layers of muddy sediments, interspersed with gravel, all of which overlie the bedrock of fractured and faulted mud-, silt- and sandstone. Brocchini et al. (2017) found that thick layers of muddy sediments were present at the MR bed surface, with fine sands near the mouth and in the lower reach of the MR. This was also confirmed by in situ samplings (REPORT - REGIONE MARCHE, 2020), carried out in 2019, showing that silt and clays dominated the riverbed composition in the upper stretch of the MR, while approaching the river mouth the percentage of sand and gravel increased. Since the final stretch of the river is highly engineered, with concrete jetties that bring the mouth of the river about 300 m seaward of the shoreline, there

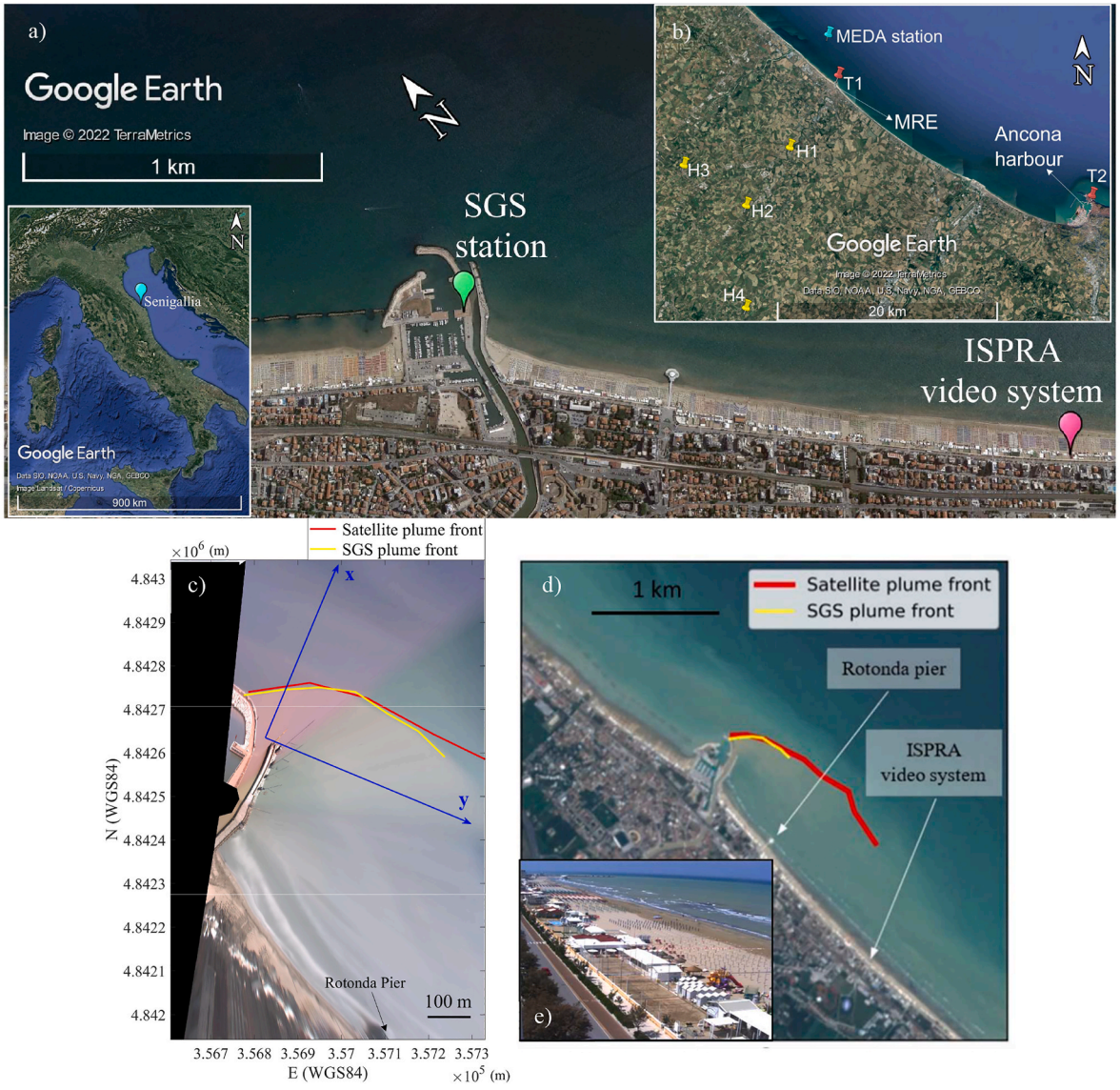

Fig. 1. a) Aerial image of the Senigallia coast, with the location of the two video-monitoring systems highlighted; b) location of the instruments used for the study (see also Table 2); c) plume front tracked from SGS (yellow line) and satellite (red line), superimposed on the Timex image of May 31 2019 (10:00 a.m.), with the blue lines identifying the reference system; d) plume front tracked from SGS (yellow line) and satellite (red line), superimposed on the satellite image of May 31, 2019 (10:08 a.m.); e) oblique image of the ISPRA video system. (For interpretation of the references to colour in this figure legend, the reader is referred to the Web version of this article.)

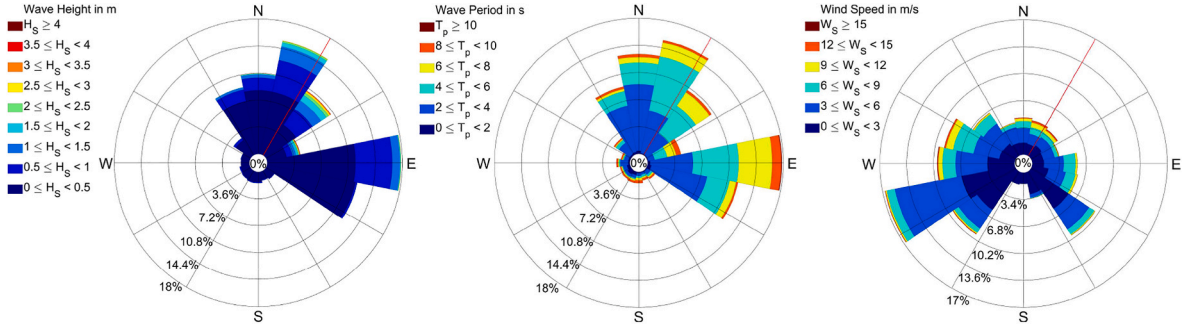

Fig. 2. Wave roses for wave significant height and wave peak period and wind rose. The red line in each rose identifies the orientation of the last stretch of the river, which is about 30°N. (For interpretation of the references to colour in this figure legend, the reader is referred to the Web version of this article.)

is no genuine prodelta region as for natural estuaries (see Fig. 4). As shown by Brocchini et al. (2017), the MR showed a cyclic behaviour with accumulation of sediment during low flow periods (summer) and expulsion of sediment to sea during high flow periods (winter). However, due to the reduced precipitation occurring over the last years, such cycle was altered, leading to the formation of an inner mouth bar frequently emerging (Baldoni et al., 2021) in the final stretch of the river.

2.2. Video-monitoring analysis and products

The MRE is monitored since 2015 by the Sena Gallica Speculator (SGS in Fig. 1a) station, deployed at the north pier of the Senigallia harbour within the EStuarine COhesive SEDiments (EsCoSed) project framework (Brocchini et al., 2017). SGS is composed of four cameras with 9 Mpx resolution, located on the top of a tower, 25 m above the mean sea level, and oriented to frame both the MRE and the 500 m-long unprotected beach between the harbour southern jetty and the Rotonda pier, with an overall field-of-view angle of around 200°. The surrounding nearshore region of MRE is contextually monitored by a second video system (https://videomonitoraggio.isprambiente.it), deployed and maintained by ISPRA (Italian Institute for Environmental Protection and Research) in order to provide information on sand bar dynamics (Fig. 1a). The monitoring stations share a similar sampling strategy, collecting images of the nearshore zone at 2 Hz for 10 min during each daylight hour (from 5:00 a.m. to 5:00 p.m. UTC) through digital video-cameras (Perugini et al., 2018; Perugini et al., 2019; Parlagreco et al., 2019). The resulting data stored consists of a set of 13 videos and 13 snapshots per day. The SGS snapshots were processed to obtain orthorectified and stabilized time exposure (Timex) images, which were used for a quantitative analysis of the plume extension. In fact, the plume front was manually tracked on the images (yellow line in Fig. 1c and d) and the offshore extent of the plume was computed as the maximum distance of the plume front from the y-axis of the local reference system chosen for the analysis (blue lines in Fig. 1c). The error associated with the manual tracking of the plume front was evaluated comparing the fronts tracked by different people for 183 cases. The mean absolute errors for the plume front and extension were about 18 m and 14.4 m, respectively, while the mean relative error for the plume extension was about 5.6%. We integrated the SGS dataset with Sentinel-2 images (Fig. 1d) to: i) visualize a wider area and ii) track the plume front (red line in Fig. 1c and d), determining its extension through the same procedure used for the SGS images. The available tiles were 100×100 km^2 ortho-images in UTM/WGS84 projection and had a temporal resolution of 5 days. For times when the two image types were available, we compared the fronts tracked from SGS and satellite, to find a good overlap.

Oblique images from the ISPRA video system (Fig. 1e), available since May 2016, were used to qualitatively correlate with the findings from SGS and satellite images and to inspect the distance reached by the plume in the southeast direction. In most cases, we found that the plume extended to the location of the ISPRA video system (2 km southward from SGS) and farther south.

The information derived from the images has been correlated with the forcing typically involved in the evolution of a river plume, described in Section 2.4: river discharge and water level, wind speed and direction, sea current magnitude and direction, sea and tidal level and wave climate.

Finally, we performed some PTV analyses on SGS videos in which floating material was visible on the surface. Such analysis allowed us to find a surface velocity associated with the plume and to look for a relation between such velocity and the plume extension. The next paragraph describes the PTV analyses and the computation of the plume velocity.

2.3. PTV analysis

2.3.1. Computation of the surface velocity field

PTV was applied to video-frames acquired by one of the cameras of the SGS station, previously processed to best adapt to the requirements of PTV analysis. In fact, we used PTV to measure velocities of floating objects visible along the last stretch of the MR. Such objects could be either wood debris or fine material, not always preserving the same shape during the period of the analysis and possibly being temporarily submerged by the waves. Thus, our "field" images did not satisfy the traditional standards for PTV analysis, which requires well-defined bright particles against a clean, dark background. Therefore, after choosing the most suitable videos, we extracted and orthorectified the frames. Then, we pre-processed the frames using image-processing techniques to make them suitable for the PTV analysis. We converted the RGB images to grayscale and applied the Matlab function Fibermetric to highlight tubular or elongated shapes, this allowing us to emphasize the visibility of the floating material. After switching the colours between background and foreground, setting a dark background and a bright foreground, we enhanced the contrast of the images. By choosing a suitable range of colours, the floating material could be further highlighted, and the noise produced mainly by wave breaking could be reduced. However, some disturbances due to waves and water ripples remained. Therefore, we applied a mask on the frames to cover the jetties and, in the most critical cases, also the stretch of river disturbed by the waves. Finally, we processed the frames using the Matlab software package Part2Track, developed at the Institute of Mechanics and Fluid Mechanics at the TU Bergakademie Freiberg (Janke et al., 2020). During the tracking operation, the software calculated the particle displacement through some user-defined parameters (e.g., particle size and brightness, field of search, etc.) and incorporated an outlier detection to enhance the quality of the displacement field reconstruction. The results by running Part2Track were a list of scattered velocity vectors for each computed frame and trajectories of the detected particles. Interpolation of the scattered data on a regular grid provided the surface velocity field. The conversion from pixels and frames to meters and seconds was performed directly by the software using the mm/px scale factor and the time separation between frames, both provided by the user. To correlate the velocity obtained with the PTV analysis with the river discharge, we extrapolated one single representative value of velocity for each video, computing a weighted mean of the velocity field, using as weights the number of particles detected by the Part2Track algorithm in each grid cell ("PTV velocity").

2.3.2. Computation of the plume velocity components

A further analysis was then performed to look for a relationship between the plume extension and velocity. Since the plume evolution was affected by a combination of factors, we decided to compute the plume surface velocity, u_{plume}, accounting not only for the action of the river, but also for the wave and wind forcing. We considered a reference system with the x-axis directed along the river (Fig. 1c) and computed the surface velocities due to the river flow, the wind and the waves at the river mouth. We decided to neglect the effect of the tide, even if it could modify the plume extension as shown in Section 4.3, because, for the analysed cases, the tidal excursion was less than $\pm$ 0.15 m. The "PTV velocity" was taken as representative of the river surface velocity, u_{river}, and pointed in the positive x-direction. The surface water velocity generated by the wind stress, u_{wind}, was related to the wind speed through a factor of 3.2% (Henderson-Sellers, 1988).

The surface water velocity due to the wave motion, u_{waves}, was computed as a Stokes drift (Van Den Bremer and Breivik, 2018), using the Ursell formula valid for general water depths:

$$u_{waves} = c(ak)^2 \cosh(2k(h+z)) \,/\, \left(2\sinh^2(kh)\right) \quad (1)$$

where $c = \sqrt{\frac{g}{k}\tanh(kh)}$ is the phase speed, $k = \frac{2\pi}{L}$ is the wave number,

$a = \frac{H}{2}$ is the wave amplitude, h is the water depth and z is the vertical coordinate (equal to zero at the free surface). The wave height H at the mouth was obtained by transferring to shore, through Delft3D, the offshore data measured at the Meda station or provided by Copernicus depending on their availability (see below); the wavelength was computed through the dispersion relation, given the water depth and the wave frequency. Both u_{wind} and u_{waves} were decomposed in the x and y-directions.

Finally, the surface plume velocity components were calculated:

$$u_{plume,x} = u_{river} + u_{waves,x} + u_{wind,x} \quad (2)$$

$$u_{plume,y} = u_{waves,y} + u_{wind,y} \quad (3)$$

Table 1 shows all the video-monitoring products used for the study.

2.4. Data collection

River water levels were obtained integrating multiple hydrometers to compensate for possible lack of data. The instruments were deployed along the Misa and Nevola (a tributary of the MR) rivers and managed by the Italian Civil Protection – Marche Region (yellow pins H1, H2, H3 and H4 in Fig. 1b). Fig. 3 shows the river water level acquired by the "Bettolelle" hydrometer (yellow pin H1 in Fig. 1b), located about 10 km upriver of the MRE, which acquires a datum of river water level every 30 min. The solid line indicates the validated data. To fill the gaps of missing data, we performed a linear interpolation (dotted line in Fig. 3). For this hydrometer, rating curves are also available to compute the river discharge.

Data of sea current speed and direction were provided by the Sontek Argonaut XR Acoustic Doppler Current Profiler (ADCP), installed in May 2016 and deployed on the Meda TeleSenigallia station (Ravaioli et al., 2017), which is about 1.5 nautical miles north of Senigallia and 1 nautical mile offshore (cyan pin in Fig. 1b), at 12.5 m depth. The up-looking bottom-mounted ADCP recorded one datum every 10 min and used 3-m cells (blank is 1 m). This instrument was substituted with the Teledyne RDI WorkHorse Sentinel ADCP 300 kHz, managed by the CNR-IRBIM (National Research Council – Institute of Marine Biological Resources and Biotechnologies), in May 2018 within the MORSE project (http://www.morse.univpm.it). Such up-looking bottom-mounted ADCP is still working, uses 1-m cells (blank is 70 cm), and measures one datum every 20 min. It was set to measure also wave climate data, providing one datum per hour. Sea current measurements are those collected at the most superficial cells, while the wave climate statistics (wave significant height, peak period and mean direction) were obtained employing cells number 1, 4, 7, 8 of the Teledyne ADCP.

The wave climate before May 2018 was derived from a multi-year wave hindcast from the Mediterranean Sea Waves oceanographic model by the E.U. Copernicus Marine Service (CMEMS) (Korres et al., 2019). Hourly-averaged values of wave data have been collected at the model node closest to the Meda station, at a water depth of around 10.5 m.

Data of wind speed and direction were supplied by the Gill WindSonic ultrasonic sensor deployed at the Meda station and provided one datum every 10 min.

The sea water level was derived from a tide gauge installed during the MORSE project within a protected area close to the entrance of the Senigallia Harbour in 2018 (red pin T1 in Fig. 1b). For earlier periods, we used online data acquired by the ISPRA Tide Station located inside the Ancona Harbour (red pin T2 in Fig. 1b), about 25 km away from Senigallia (see www.mareografico.it). The two signals are in good and continuous agreement. The Ancona and Senigallia tide gauges record water level data every 10 and 6 min, respectively, and their elevation datum is the mean sea level. In addition, the astronomical component of the tide was derived from the total signal recorded by the Ancona gauge using the tidal analysis of Delft3D Tide module. Table 2 reports the complete list of instrumentation.

Table 1
Video monitoring products used for the analysis.

Data type	Time coverage	Acquisition frequency	Use
SGS images	2016–2019	13 images/day (5 a.m. - 5 p.m.)	plume tracking/plume offshore extension computation
Satellite images	2016–2019	1 image/5 days	plume tracking/plume offshore extension computation
ISPRA images	2016–2019	13 images/day (5 a.m. - 5 p.m.)	qualitative inspection of the plume southward alongshore extension
SGS videos	2016–2019	13 videos/day[a] (10-min duration)	PTV analysis, computation of the river surface velocity

[a] We chose some videos where floating material was visible.

Table 2
Instruments used for the analysis.

Data type	Instruments	Time coverage	Temporal resolution	Use
Water level	Hydrometer H1 (Bettolelle)	2014–2019	30 min	correlate with plume occurrence
	Hydrometer H2	2015–2019		
	Hydrometer H3	2014–2019		
	Hydrometer H4	2014–2019		
River discharge	Rating curve of hydrometer H1	2014–2019	30 min	correlate with plume occurrence and PTV data/ input for simulations/ model calibration
Wave data	ADCP (EsCoSed experiment)	Jan 2014	1 h	model calibration
	CMEMS	2016–2018	1 h	correlate with plume occurrence and PTV data/ input for simulations
	Teledyne ADCP (Meda station)	2018–2019	1 h	
Sea water level	Ancona tide gauge T1	2014–2018	10 min	correlate with plume occurrence/input for simulations/ model calibration
	Senigallia tide gauge T2	2018–2019	6 min	
Astronomic tide	Delft3D tide module	2014–2019	same as the input signal	correlate with plume occurrence
Wind	Weather station	Jan 2014	15 min	model calibration
	Gill WindSonic sensor (Meda station)	2016–2019	10 min	correlate with plume occurrence and PTV data/ input for simulations
Sea current	Sontek ADCP (Meda station)	2016–2018	10 min	correlate with plume occurrence
	Teledyne ADCP (Meda station)	2018–2019	20 min	

2.5. Numerical simulations

Hydro-morphodynamic simulations were performed using the Delft3D software suite (Lesser et al., 2004; Deltares, 2014, 2019), a widely used 3D modelling suite to investigate hydrodynamics, sediment transport and morphology for fluvial, estuarine and coastal environments. A two-dimensional (2D), depth-averaged, model was

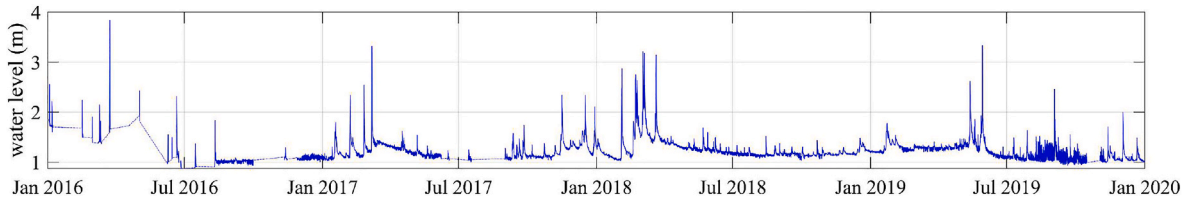

Fig. 3. River water level timeseries for "Bettolelle" hydrometer (H1 in Fig. 1b). The solid and dotted lines represent, respectively, the validated data and the linearly interpolated data.

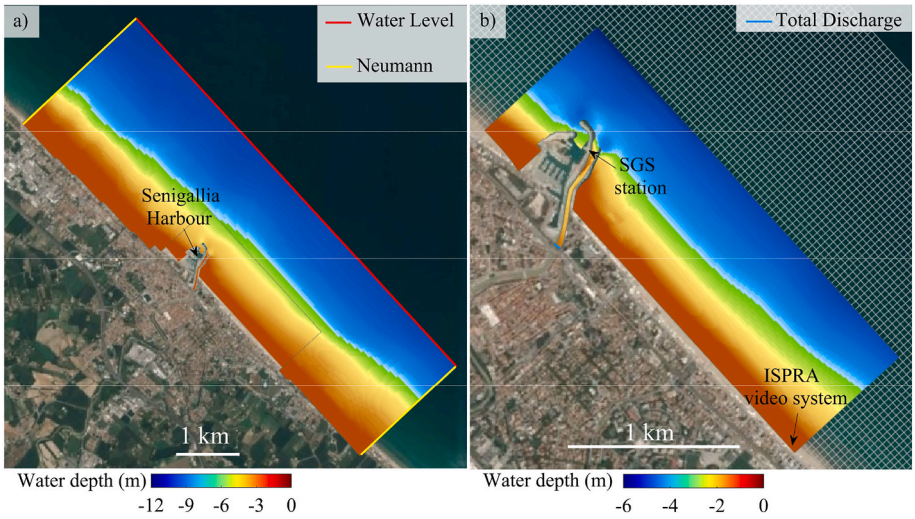

Fig. 4. Overview of the numerical model grids. Location and type of the boundary conditions for the FLOW simulation in the coarser grid (a) and in the finer grid (b). The colorbars indicate the water depth, negative downward.

implemented coupling the FLOW and WAVE modules. We chose to run 2D simulations because our focus was on the planar extension of the plume toward the offshore and alongshore and not on the vertical structure of the plume. Two regular grids, made by rectangular elements aligned with the coastline and the river axis, were created (Fig. 4).

As standard for Delft3D, WAVE computations were run nesting a finer grid into a larger one, whereas FLOW computations were performed using the domain decomposition approach. The larger grid covered the coastal area in front of the Senigallia Harbour, it had a spatial resolution of 33.3 × 33.3 m^2 and extended about 7.8 km in the alongshore direction and 2.5 km in the offshore direction. The finer grid covered the final stretch of the MR and extended southwards reaching the beach in front of the ISPRA video system.

It had grid cell size variable from around 8.3 m in the offshore region to around 3.0 m along the river and it extended about 2.5 km in the alongshore direction and 0.8 km in the offshore direction. The reference system used for the simulations was Monte Mario/Italy Zona2. After conducting a model calibration, we performed two real-life simulations by online coupling Delft3D-FLOW with Delft3D-WAVE, forcing the model with the real field conditions described in Section 2.4. The WAVE model was forced with timeseries of wave parameters at the seaward boundary of the larger grid. For the FLOW model, a total of four boundaries were defined. In the finer grid, a total discharge boundary condition was used in the upstream boundary of the river channel (Fig. 4b). In the same section, a cohesive sediment concentration was imposed as defined in Section 2.5.1. The offshore boundary of the larger grid computation was forced with a water level timeseries, using data recorded by the Senigallia tide gauge. At the two cross-shore boundaries, zero-gradient water level (Neumann-type) boundary conditions were specified (Fig. 4a). Moreover, wind timeseries, uniformly distributed over the domain, were used as input forcing. We chose not to implement marine currents due to the Adriatic global circulation (e.g. Western Adriatic Currents) because the available data, acquired about 1 nautical mile offshore from the MRE and displaying a decreasing intensity toward the shoreline, would represent a very minor agent for the plume evolution. The primary role of the wind rather than the coastal circulation in affecting small plume evolution is also documented in literature (Ostrander et al., 2008; Osadchiev and Sedakov, 2019). Finally, we added a background concentration for the Northern Adriatic Sea equal to 0.05 kg/m^3 (Harris et al., 2008; Brando et al., 2015).

The bathymetry was created by interpolating at the grid nodes the depth values coming from both the EMODnet bathymetry, available online, and a multibeam bathymetric survey of 1 m resolution carried out by the municipality of Senigallia in 2018. The survey extended 1 km offshore from the coastline, up to around 6 m depth, and 2.5 km in the alongshore direction, being the MRE at the center of the survey.

The bed stratigraphy was modelled using one mixed layer composed of a space-variable mix of gravel, fine sand and cohesive sediment. Based on in situ samplings (Report – Marche Region, 2020), the upper stretch of the MR was characterized with 100% cohesive sediments, then, the presence of silt and clay decreased seaward until reaching 100% of sand in the sea area. Moreover, in the last stretch of the river, in correspondence of the inner bar location (Baldoni et al., 2021), a small percentage of gravel was added (2–3%). The sand and the gravel were characterized using a D_{50} of 0.18 mm and 6 mm, respectively, while for the cohesive sediments we set the critical shear stress for erosion equal to 0.3 N/m^2, the critical shear stress for deposition equal to 0.4 N/m^2 and the erosion parameter equal to 10^{-4} kg/m^2/s (see Table 3). A 12-h spin-up interval, during which the model did not perform any morphological update, was used.

2.5.1. Calibration of the model morphological parameters

The hydrodynamics of the model was already calibrated in Baldoni et al. (2021), where the capabilities of the model to well describe the

Table 3
Parameters used for the simulations.

Parameter	Tested values	Model value
Manning coefficient ($m^{-1/3}/s$)	0.008–0.03	0.015
Background horizontal eddy viscosity (m^2/s)	0.5–5	1
Background horizontal eddy diffusivity (m^2/s)	1–20	10
Critical shear stress for erosion (N/m^2)	0.1–0.5	0.3
Critical shear stress for sedimentation (N/m^2)	0.4–1000	0.4
Settling velocity (mm/s)	0.005–0.1	0.1
Erosion parameter ($kg/m^2/s$)	1e-5 – 1e-3	1e-4
Calibration factor for bedload by currents (−)	0.2–1	0.2
Calibration factor for suspended load by currents (−)	0.2–1	0.2
Calibration factor for bedload by waves (−)	0.2–1	0.4
Calibration factor for suspended load by waves (−)	0.2–1	0.4

evolution of the riverbed under different forcing were also shown. Here, we verified that the parameters used in Baldoni et al. (2021) were appropriate also for the description of the plume evolution and the suspended sediment transport. We tuned some parameters, shown in Table 3, and compared the results with some available measures, relative to an experiment carried out in January 2014 (Brocchini et al., 2017). The WAVE model was forced using wave parameters timeseries provided by an ADCP, deployed for the experiment and located 900 m offshore. The FLOW module was forced using river discharge timeseries at the river section, Neumann conditions at the two cross-shore boundaries, and water level timeseries of the Ancona tide gauge at the offshore boundary. Moreover, wind timeseries collected by a weather station located on top of the harbour lighthouse were also employed.

The bathymetry was created by interpolating at the grid nodes the depth values coming from both the EMODnet bathymetry, available online, and a multibeam survey performed in the lower reach of the MRE before the experiment. The survey was conducted using an ODOM ES3 operating at 240 kHz and had a resolution of 0.7 m. It covered an area of about 400 m^2 around the estuary, up to around 4 m depth, and the final stretch of the river. Additional details can be found in Brocchini et al. (2017).

During the experiment, vertical profiles of turbidity were recorded by hand-deploying a Hach Quanta Hydrolab® at regular intervals in the river and the estuary. We converted the depth-averaged turbidity measures to suspended solid concentration (SSC), using a conversion factor of 1 NTU = 10 mg/l, to compare with simulation results. Based on previous MR studies, high SSC are in the region of 2500 mg/l and this was deemed equivalent to the maximum turbidity measured during the experiment, 250 NTUs (Postacchini et al., 2022).

The plume was the result of both sediment transported by the river from the upstream part of the basin to the mouth and sediment suspended locally in the final stretch of the river by the river current and the waves. For that reason, an input concentration of the cohesive sediment fraction was used at the upstream boundary of the river channel in this calibration and in the real-life cases. Such concentration was related to the river discharge using a power rating curve of the type $C = aQ^b$ for the sediment (Asselman, 2000; De Girolamo et al., 2015). We imposed $b = 1$, which is a reasonable value for Mediterranean small rivers characterized by relevant differences among mean daily flows and the extreme instantaneous flows during floods. Then, we found $a = 1/3$ as the value that best fitted the observed concentration values. Such values were also in agreement with some historical data for the sediment transport in the Marche Region provided by AQUATER - REGIONE MARCHE (1982).

We evaluated the response of the modelled velocities and suspended sediment concentration (cohesive fraction) to the variation of the user-defined parameters shown in Table 3. We considered two points located respectively along the river channel and in the sea in front of the MR mouth. The parameters that most affected the velocities were the Manning coefficient and the background horizontal eddy viscosity, while the concentration was mostly dependent on the critical shear stress for sedimentation, the Manning coefficient and the background horizontal eddy diffusivity. Both velocities and concentration showed higher variability in the sea rather than the river. Table 3 shows the range of values tested for each parameter and the calibrated model parameters.

3. Results

We correlated the occurrence and extension of plumes derived from the images with the data presented in Section 2.4 to identify the main generation and transport mechanisms. Fig. 5 shows an example of the resulting classification of plume events based on their generation mechanisms, where the red, green and blue rectangles highlight plumes due to NNE waves only, a combination of river discharge and waves and E waves only, respectively. Moreover, we identified on the images the main characteristics of each type of plume. At the end of the analysis, we could distinguish two generation mechanisms (see Section 4.1), the river discharge and the waves, and some mechanisms of sediment transport (see Section 4.2), the wind, the waves and the currents. Then, we simulated two events that highlighted well the identified mechanisms and their differences, as regard the suspended concentration and the plume extension.

3.1. Real-life cases: observation and simulation results

We present results for an event generated by a river discharge (RD case) and an event generated by waves coming from NNE (W case), combining the observed data and the numerical simulations. It is clearly difficult to associate real-life events purely to one single mechanism, as often they are the outcome of a combination of physical phenomena. The events described in this section are, therefore, those that were characterized by the prevalence of one generation mechanism over the others. Parametric events, modelled using one single prevailing forcing, are discussed in Section 4. Moreover, we selected two events well visible in both SGS and satellite images, to track the plume front. Finally, we run Delft3D numerical simulations forced using recorded timeseries (Section 2.4 and Section 2.5) to compare the modelled and observed plume shapes and to highlight the differences between the RD and W cases.

The RD case occurred on 29–31 May 2019 and was generated by a river discharge that reached 106 m^3/s on May 29, 2019, at 6:30 p.m. The

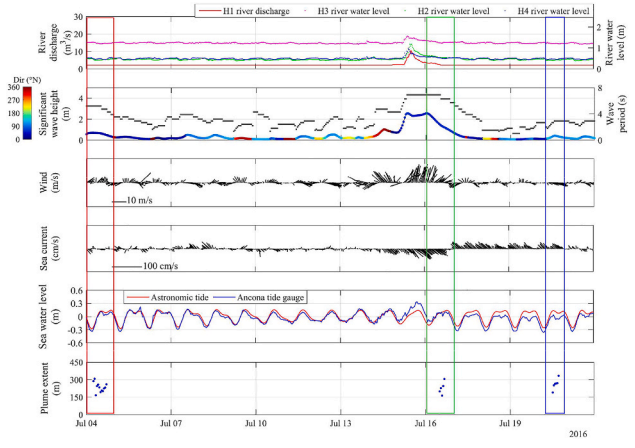

Fig. 5. Example of the forcing timeseries used to correlate generation mechanisms with the river plume occurrence and extent. Red, green and blue rectangles highlighted three plume events, generated by NNE waves, a combination of river discharge and waves and E waves, respectively. In the top panel, H1, H2, H3, H4 represent the different hydrometers used for the analysis (see Section 2.4), indicated in Fig. 1b. (For interpretation of the references to colour in this figure legend, the reader is referred to the Web version of this article.)

wave climate was characterized by a maximum significant wave height of 0.91 m, comparable with the 90th percentile of the observations, and variable direction, mainly N and NE. Fig. 1c and d show the plume from the SGS Timex image and from the satellite image, both acquired on May 31, 2019, at 10:00 a.m. and 10:08 a.m. respectively. Since this plume occurred about two days after the discharge event, a large quantity of sediment had already been washed out from the estuary, as confirmed by the bright area extending parallel to the coast. However, a dense plume could be distinguished from the background, meaning that the effect of the river discharge was still important after two days.

The images showed that the plume was directed toward SE, this meaning that the prevailing transport mechanism was the wind coming from N-NNW at a maximum speed of about 9 m/s. Such value corresponded to the 95th percentile of the observations. The sea current, directed toward NW, did not affect the plume direction in this case. The dominance of the wind forcing in determining the plume evolution is reported in various observational and modelling studies, for both large (e.g. Fong and Geyer, 2001; Janzen and Wong, 2002; Whitney and Garvine, 2005; Choi and Wilkin, 2007) and small river systems (e.g. Piñones et al., 2005; Osadchiev and Sedakov, 2019; Cyriac et al., 2020). Ostrander et al. (2008) found a strong correlation between drifters and wind direction in a river characterized by outflows ranging between 50 and 100 m^3/s, similar to the MR, meaning that the surface water responded directly to the forcing of the wind, moving along its heading.

Fig. 6a shows the map of the modelled suspended sediment concentration (dominated by the cohesive fraction, as illustrated in Section 4). The simulated plume deflected toward SE, as in the images, and the tracked fronts fell between 0.1 and 0.07 concentration isolines, which reached the nearshore region in front of the ISPRA video system.

The W wave case occurred on 11–13 March 2019 and was characterized by a low river discharge of about 2 m^3/s and by N-NNE waves reaching 2 m, comparable to the 99th percentile of the observations, on March 11, 2019 at 10:00 p.m. The SGS and satellite images (reported in the Supplementary material) showed a light plume and breaking waves, which caused sand resuspension in the surf zone that mixed with the plume. Fig. 6b shows the modelled suspended sediment concentration. The high concentrations near the shoreline were caused by the resuspension of the sand due to the wave action, while near the river mouth the plume was mainly composed by cohesive sediment. The simulation confirmed a density of the plume smaller than that generated by the river discharge, the plume front falling in correspondence of the 0.059 concentration isoline, which is about a half of the value found for the RD case, and quantifying the marked density difference between the two types of plumes. The offshore extent of the W plume was around 30 m smaller than that of the RD case, restrained near the coast by the action of the waves. The wind coming from NNW contributed to the spreading of the plume mostly toward SE, as shown by the isolines.

The fate of the plume for these real-life cases has also been characterized by means of the conceptual model of Kastner et al. (2019). The RD case was seen to be bathymetry-dominated, since the length of the channel (L_C = 300 m) was larger than both the width of the surf zone (L_{SZ} = 42 m) and the near-field plume length (L_{NF} = 70 m). In such conditions, wave breaking occurred inshore of the ends of the jetties and caused no opposition to the river momentum, thus the river water could escape from the surf zone (Fig. 6a). Conversely, the W case was wave-dominated, with L_{SZ} = 383 m larger than both L_C = 300 m and L_{NF} = 26 m. With such conditions, the plume was trapped in the surf zone because the wave-driven momentum, directly related to wave breaking, dominated over the river momentum. To confirm this statement, we computed the dimensionless parameter S_w (wave stress ratio), following an approach similar to that by Zarzuelo et al. (2021). For our system, such parameter represented the ratio between the river and the wave actions and was defined by scaling the terms of the momentum equation related to such forces. The numerator was scaled as U^2/L, where U is the river depth averaged velocity and L is a length scale defined as the distance between the river section of the model and the river mouth. Melito et al. (2020) showed that sea/swell waves are strongly dissipated before entering the river mouth and only infragravity waves do propagate upstream. The denominator was scaled as $F_s/\rho_0 h$, where F_s is the wave induced force per unit area and ρ_0 is the water reference density. All quantities were evaluated at the river mouth using the numerical results at the peak of each event. The sign of the base 10 logarithm of S_w gave the greater importance of numerator or denominator. We found a positive value for the RD case, meaning that the river forcing prevailed over the waves, while a negative value was obtained for the W case, indicating wave prevalence. Moreover, given the high engineering of the MR, the role of the jetties strongly influenced the plume behaviour, as shown by a further analysis, performed by varying the wave parameters and keeping the river discharge fixed ($Q = 2\ m^3/s$) and vice versa (with fixed $H_s = 0.5$ m and $T = 5$ s). We found channel dominant conditions for all the RD cases tested and for the W cases characterized by $H_s \leq 1.6$ m. On the other hand, the W cases with $H_s \geq 2.4$ m were wave-dominated regardless of the wave period, while for H_s in the range $1.7 \div 2.3$ m, wave dominant conditions occurred only for some combinations of significant wave height and period, with larger periods being needed at the decrease of the wave height.

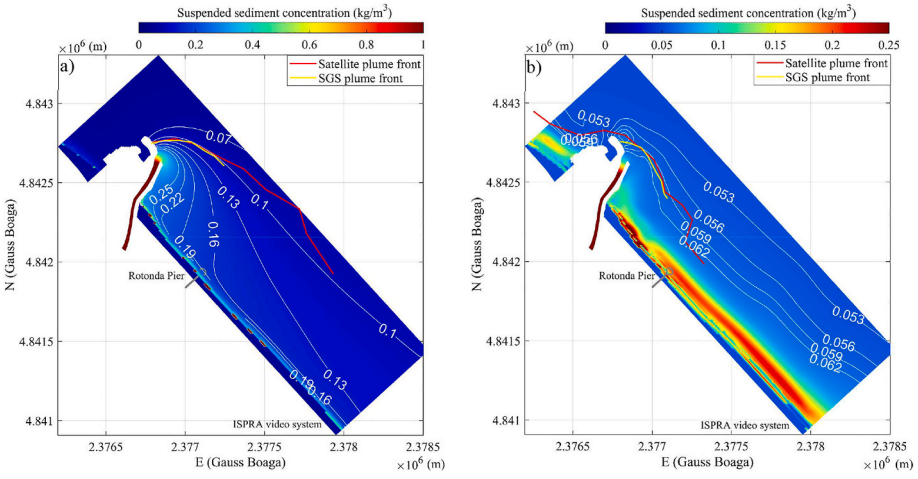

Fig. 6. Maps of the modelled suspended sediment concentration with some white contour lines for a) RD case and b) W case. In both the images, the fronts of the plume drawn on the SGS image (yellow) and on the satellite image (red) have been reported. (For interpretation of the references to colour in this figure legend, the reader is referred to the Web version of this article.)

Table 4
List of the analysed videos and forcing: the river discharge (Q), the wave parameters (H_s, T_p and wave dir.), the wind speed and direction (wind speed, wind dir.). The wave parameters (significant height, peak period and direction) were transferred to the river mouth through the Delft3D wave module. The last column reports the plume offshore extensions.

video ID	video date	Q	H_s	T_p	Wave dir.	Wind speed	Wind dir.	Extent
		m^3/s	m	s	°N	m/s	°N	m
EV1	Mar 23, 2016 11 a.m.	81.50	1.67	7.37	44.13	12.7	16.8	–
EV2	Apr 25, 2016 10 a.m.	18.44	1.44	5.74	39.64	8.31	357	147
EV3	May 02, 2016 11 a.m.	32.95	0.54	5.74	18.55	5.23	313	456
EV4	May 20, 2016 02 p.m.	18.44	1.03	5.07	35.22	5.96	339	353
EV5	Jun 20, 2016 04 p.m.	22.79	0.42	4.47	17.37	5.15	299	489
EV6	Mar 07, 2017 12 p.m.	70.36	1.51	6.5	40.43	9.86	308	388
EV7	Feb 03, 2018 08 a.m.	29.47	0.85	6.5	32.99	10	300	379
EV8	Mar 21, 2018 09 a.m.	49.92	1.6	7.37	42.31	13	214	800
EV9	May 14, 2019 09 a.m.	17.63	1.55	8.35	45.11	4.65	31.9	800

3.2. PTV results

To study the complex dynamics of the MRE, characterized by a combination of forces, we conducted PTV analyses on some video-recordings. Among all the available data, we selected events where floating material, detectable by the PTV, was clearly visible on the river surface (Table 4). To correlate the velocity derived from the PTV analysis with the river discharge (Table 4), we extrapolated a weighted mean velocity for each video, as discussed in Section 2.3.1. Such value, hereinafter named "PTV velocity", was compared with a "manual velocity" that indicated the mean velocity of some particles that we manually tracked on each video. The "manual velocities" were.

Used to check the accuracy of the PTV results, which were characterized by a relative error in the range 0.8–33%. Fig. 7 shows the "PTV velocity" and the "manual velocity" with dots and asterisks, respectively, and their correlation with the river discharge. The surface velocities increased with the river discharge through a parabolic dependence ($v = -0.00027Q^2 + 0.067Q - 0.037$). The R^2 coefficients are 0.77 and 0.87, respectively, for the "PTV velocity" and "manual velocity". The data scattering was due to the several forcing that acted in the estuarine area, e.g. wind, waves and tide, and that affected the surface velocity. Finally, we computed the mean velocities of some drifters, launched within the EsCoSed project in 2014 (see Brocchini et al., 2017), to compare their values with the PTV ones. The mean calculation was limited to the portion of the drifter trajectories that fell within the area framed by the video-images. Such values (triangles in Fig. 7) were in good agreement with the fitting curve, confirming the reliability of the PTV analyses also for low velocities, which are characterized by the largest relative errors.

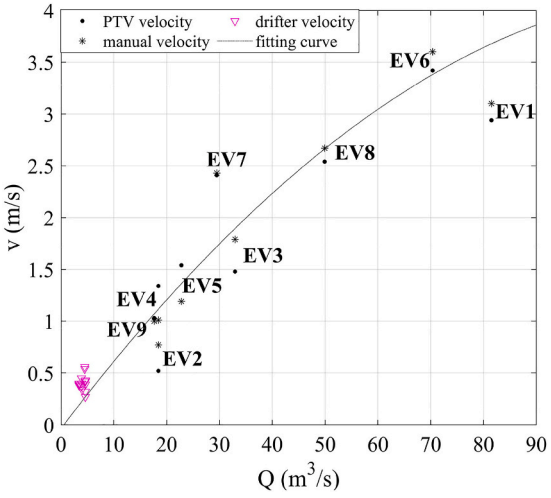

Fig. 7. Correlation between particle velocity (v) and river discharge (Q). Dots and asterisks identify the PTV velocity and the manual velocity, respectively; the triangles represent the drifter velocity. The dotted line is the fitting curve for the PTV velocity data.

However, the action of the river was not the only force to affect the plume evolution. At a river mouth, the interplay of multiple factors determined the velocity of the flow and the consequent extension of the plume. Therefore, we performed a further analysis to compute the plume surface velocity, u_{plume}, accounting not only for the action of the river, but also for the wave and wind forcing (Table 4). The computations are explained in Section 2.3.2 and provided the result shown in Fig. 8. Events EV1 and EV9 were discarded because either it was not possible to track the plume front due to poor image quality or the video was not in phase with the discharge peak, this impeding association of the plume velocity and extension (the latter influenced by the previous discharge).

Fig. 8a shows the contributions giving the component of the plume surface velocity in the alongriver direction ($u_{plume,x}$). They are positive or negative if directed from the river toward the sea or vice versa. For the seven analysed events, the main forcing was u_{river}, which was on average about an order of magnitude larger than $u_{waves,x}$ and two order of magnitude larger than $u_{wind,x}$. Waves always opposed the river action, this suppressing the offshore propagation of the plume, as also observed by Rodriguez et al. (2018). The wind could either contrast or enhance the river action depending on its direction. For the analysed events, the wind contributed to the river action only for EV8.

The contributions affecting the component of the plume surface velocity in the alongshore direction ($u_{plume,y}$) are illustrated in Fig. 8b, positive/negative if directed toward SE/NW. The major forcing was $u_{wind,y}$, which was on average an order of magnitude larger than $u_{waves,y}$. The alongshore component of the waves is usually mild because refraction makes the wave fronts almost parallel to the coast. In fact, $u_{waves,x}$ was on average 7 times larger than $u_{waves,y}$. The ratio between the alongshore and cross-shore components of the wind is more variable because it depends on the wind direction.

The sum of all contributions provided the components of the plume surface velocity, shown in Fig. 8c. $u_{plume,x}$ was generally larger than $u_{plume,y}$, which was directed mainly toward SE. We believe that the extension of the plume is determined by the combination of the two velocity components, meaning that it depends on both the magnitude and direction of the plume velocity. Therefore, we correlated the plume extension with the absolute value of the ratio between $u_{plume,x}$ and $u_{plume,y}$, which represents the angle of the resulting velocity vector with the x-axis (Fig. 1c). The correlation coefficient between the two variables represented in Fig. 8d was 0.87, meaning that they were strongly correlated. Thus, for fixed $u_{plume,y}$, the plume extension increased with $u_{plume,x}$, largely determined by the river velocity. Such result was expected since many authors found a direct proportionality between the river force and the plume extent (e.g., Lebedev et al., 2020). On the other hand, for fixed $u_{plume,x}$, the plume extension decreased for increasing $u_{plume,y}$ because the alongshore current due to waves and wind deviated the plume toward either SE or NW, limiting its offshore extension (see Section 4.1 and Section 4.2). Moreover, being $u_{plume,y}$ mainly due to the

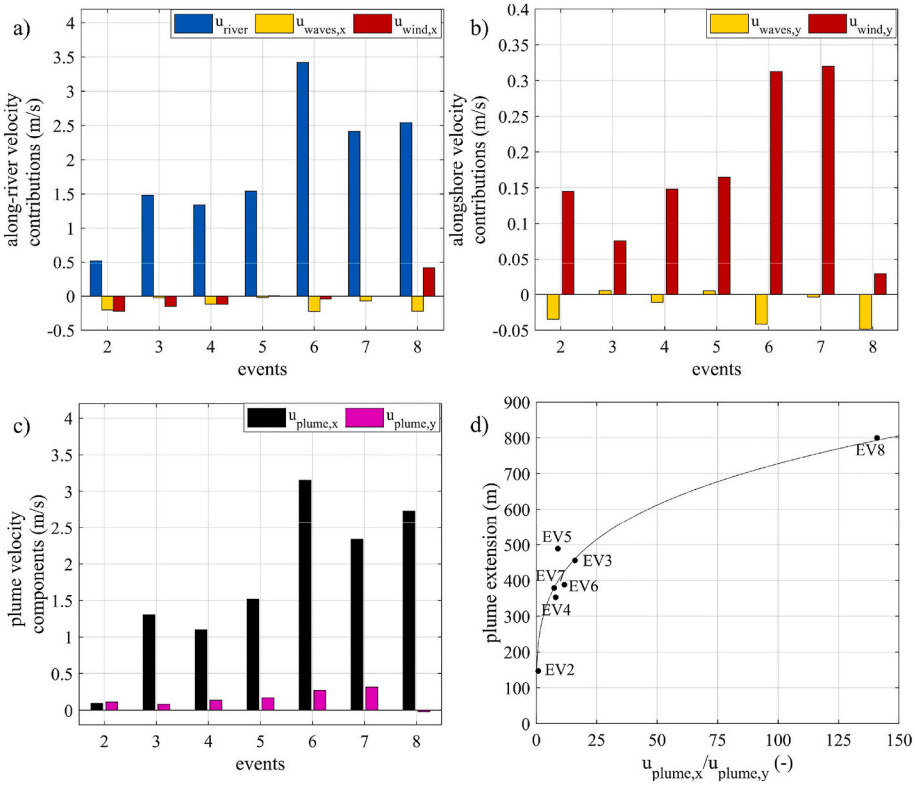

Fig. 8. a) contributions of river (blu), waves (yellow) and wind (red) to the alongriver plume velocity. b) contribution of waves (yellow) and wind (red) to the alongshore plume velocity. c) components of the plume surface velocity in the alongriver (black) and alongshore (magenta) directions. d) correlation between the plume extension and the ratio between $u_{plume,x}$ and $u_{plume,y}$. (For interpretation of the references to colour in this figure legend, the reader is referred to the Web version of this article.)

wind forcing, the more the wind blowed parallel to the coast the smallest was the plume extent, as also found in Section 4.2. A similar result was usually observed in microtidal small systems like the MRE (Ostrander et al., 2008; Osadchiev and Sedakov, 2019). The relation linking the two variables of Fig. 8d was a power law with $R^2 = 0.93$:

$$e\left(\frac{u_{plume,x}}{u_{plume,y}}\right) = 230.2\left(\frac{u_{plume,x}}{u_{plume,y}}\right)^{1/4} \quad (4)$$

where e is the plume extension.

Equation (4) can be used to estimate the plume offshore extension known the main forcing acting in the estuarine area, i.e. river discharge, waves and wind.

4. Discussion

Field observation allowed us to identify both plume generation and transport mechanisms. In a natural environment, the action of a specific forcing is difficult to isolate, since typically the observed physical phenomena are the outcome of a combination of several mechanisms.

To inspect the role of the different generation mechanisms separately one from another, we run parametric simulations using artificially-built conditions reproducing the shape of typical flood hydrographs and storms. For the wave direction we chose NNE and E, being the most frequent storms impacting on the Senigallia coast from these directions. At the offshore boundary a zero-water level condition was imposed to neglect the effect of the tide. We run simulations to verify that both river discharge and waves can suspend sediments inside the river mouth. Thus, we did not add an input concentration in such simulations and only accounted for the local generation of the plume. However, we still considered a background concentration of 0.05 kg/m^3 typical of the Northern Adriatic.

We performed three simulations forced only by river discharge timeseries, characterized by discharge peaks of 10 (RD 10), 50 (RD 50) and 100 m^3/s (RD 100) and shape similar to real-life discharge events, and four simulations forced only by waves, characterized by maximum wave heights of 2 and 4 m and by directions equal to 20°N and 90°N (W NNE 2, W NNE 4, W E 2, W E 4).

Then, we run simulations all forced by the 50 m^3/s river discharge peak, comparable with a discharge with a return period shorter than 1-year, but associated with a uniformly distributed and constant wind coming from different directions, to study the effect of the wind on the plume direction. The wind intensity was fixed at 10 m/s, while the investigated wind directions were 30, 135, 210 and 315°N, to observe the effect of winds directed toward the coast, NW, the offshore and SE, respectively (RD 50 wind 30, RD 50 wind 135, RD 50 wind 210, RD 50 wind 315). We associated the wind also with simulations forced by waves ($H_s = 4$ m), imposing a wind direction in agreement with that of the waves (W NNE 4 wind 20, W E 4 wind 90). Finally, two simulations were run to inspect the role of high and low tide coupled with the 50 m^3/

Table 5
Overview of the parametric simulations.

	USED FORCING			
simulation ID	river discharge (m^3/s)	wave dir/height (m)	wind dir (°)	tide
RD 10	10	–	–	–
RD 50	50	–	–	–
RD 100	100	–	–	–
W NNE 2	–	NNE/2	–	–
W NNE 4	–	NNE/4	–	–
W E 2	–	E/2	–	–
W E 4	–	E/4	–	–
RD 50 wind 30	50	–	30	–
RD 50 wind 135	50	–	135	–
RD 50 wind 210	50	–	210	–
RD 50 wind 315	50	–	315	–
W NNE 4 wind 20	–	NNE/4	20	–
W E 4 wind 90	–	E/4	90	–
RD 50 ht	50	–	–	high
RD 50 lt	50	–	–	low

s river discharge peak. This was done by creating a sinusoidal timeseries for the tide and by making the peak of the river discharge timeseries simultaneous once with the high tide and once with the low tide (RD 50 ht, RD 50 lt). Table 5 shows an overview of all the parametric simulations performed.

4.1. Generation mechanisms

Two main mechanisms for the plume formation, i.e. mechanisms that directly put the riverbed sediments into suspension, were recognised: the river discharge (RD) and the waves (W). The occurrence of a river discharge was always followed by a dense plume flowing out from the estuary mouth (Fig. 9a). Such plume appeared well marked in the images and we could recognize it clearly, since it caused a distinct change in the water colour from blue to brown. The high sediment.

Concentration derived from: i) the material eroded and transported by the river from the upstream part of the basin to the mouth and ii) the local sediment suspended by the action of the river discharge. However, in the parametric simulations, we chose to inspect only the local generation of the plume at the river mouth, thus the following results show the concentration of cohesive sediments suspended in the final stretch of the river mouth by different forcings. We retained only the cohesive concentration because it was an order of magnitude larger than that of the sand and we made it dimensionless using the representative background concentration for the Northern Adriatic, $c_{ref} = 0.05$ kg/m^3. Therefore, the plume was identified as the area where the dimensionless concentration exceeded 1.

The discharge threshold above which sediment suspension began, identified as the minimum river discharge that led to exceeding the model critical shear stress for erosion (0.3 N/m^2), was 12 m^3/s. Above such value, the plume extension increased with the river discharge (Fig. 9d), this in agreement with the literature (Mestres et al., 2007; Osadchiev and Sedakov, 2019; Lebedev et al., 2020). Trying to apply a linear regression between the river discharge and plume extension, similarly to Lebedev et al. (2020), we obtained a correlation coefficient of 0.95. Such results are also in agreement with the findings of Section 3.2, where the plume extent, other factors being equal, was found to increase with the plume alongriver velocity (Fig. 8d), which in turn was proportional to the river discharge (Fig. 7). The suspended concentration also increased with the river discharge, with maximum values occurring in the final stretch of the river, where the riverbed was characterized by a large deposit that caused the reduction of the section and the consequent increase of the velocity and of the bed shear stress. At such location, at peak time, the concentration was about 5 and 11 times the reference one, respectively for the 50 and 100 m^3/s river discharge peaks. The reader can refer to the figures in the Supplementary material.

Plume events forced by waves coming from E and NNE were caused by the important stirring action of the riverbed sediments at the river mouth and appeared less dense than RD ones. NNE wave-forced plumes spread around the river mouth, frequently assuming an arched shape immediately after exiting the river mouth (Fig. 9c), while E wave-forced plume deviated toward NW (Fig. 9b).

Fig. 9e and f display the plume fronts at storm peak for E and NNE waves. Blue and red lines refer to $H_{s,max} = 2$ m and $H_{s,max} = 4$ m, respectively. NNE waves, approaching the coast perpendicularly to the MRE, easily entered the estuary causing an increase of both flow and bed shear stress up to about 190 m upriver, while E waves entered the estuary to a smaller extent. The maps of the bed shear stress can be found in the Supplementary material.

The storm characterized by $H_{s,max} = 4$ m, comparable with a 5-year return period storm, regardless of the direction, forced a shear stress about a half of that by the simulation with a 50 m^3/s peak discharge, associated to a return period smaller than 1 year. This means that a yearly-typical river discharge generated a riverbed erosion more intense than that triggered by a 5-year return period wave storm. Thus, the concentration generated by the waves was smaller than the concentration resulting from the 50 m^3/s peak discharge simulation. This agrees with the findings of Baldoni et al. (2021), who observed that the migration of the MR inner bar was more affected by river discharges,

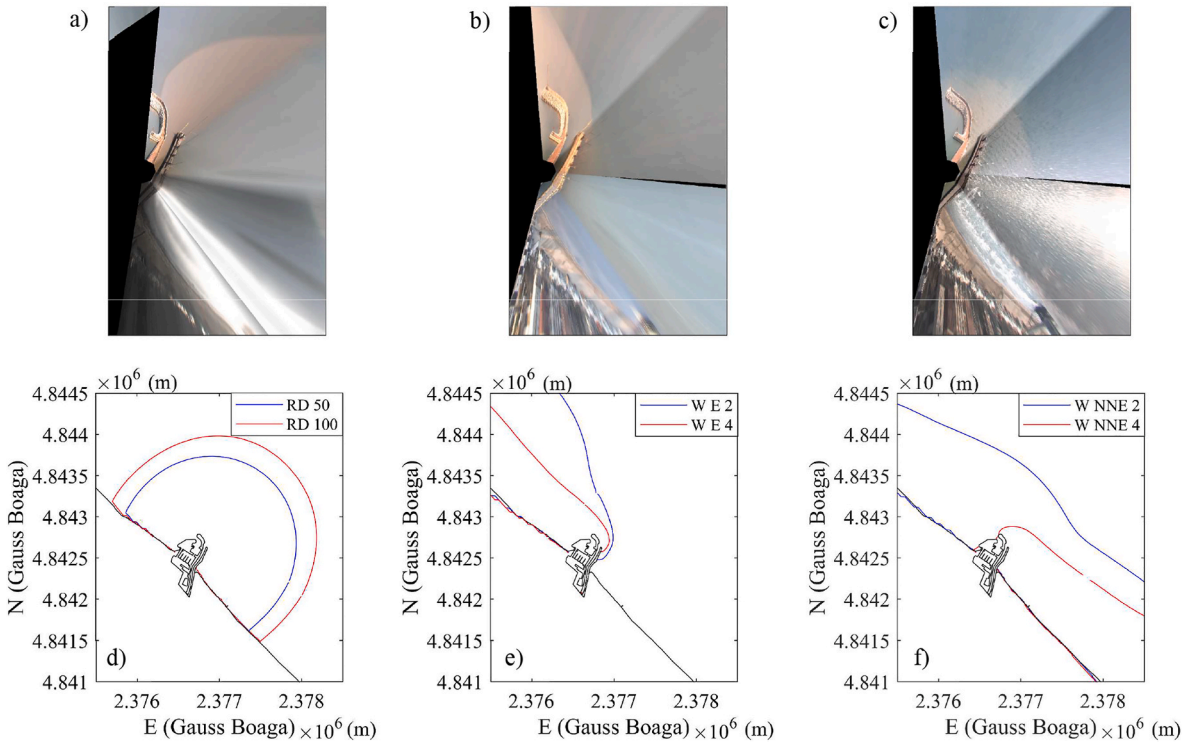

Fig. 9. In the top row, SGS images of: a) a RD-generated plume, b) a E wave-generated plume, c) a NNE wave-generated plume. In the bottom row, plume fronts resulting from the simulations forced with: d) river discharge, e) E waves, f) NNE waves.

even if small, than intense storm waves.

Results also showed that alongshore currents due to waves represented a transport mechanism for the plume (Kastner et al., 2019). Fig. 9e and f show that when wave-generated currents were mild, i.e.for $H_{s,max} = 2$ m, the plume was more extended toward the offshore (blue lines). In particular, under small NNE waves, the plume remained symmetrically diffused around the estuary. Instead, intense wave-generated currents, i.e. those caused by $H_{s,max} = 4$ m, deviated the plume in the alongshore direction reducing its offshore extent (red lines). Such nearshore constraining action of sea waves on river flows is also described in the literature of which Olabarrieta et al. (2014) is a good example.

4.2. Transport mechanisms

The direction of sediments put in suspension by the mechanisms above was mainly governed by the wind, the waves and the sea currents, whose directions were mostly in good agreement, and all contributed to alongshore deflect the plume. In cases when winds and sea currents were discordant, like the real-life cases of Section 3.1, the plume typically followed the wind direction rather than that of the current, highlighting the dominance of the wind forcing among the transport mechanisms in small rivers (Ostrander et al., 2008; Osadchiev and Sedakov, 2019).

Fig. 10a shows the plume fronts resulting from the simulations forced with a river discharge peak of 50 m^3/s and winds coming from different directions (Table 5). South-easterly and north-westerly winds, blowing along the coast, deflected the plume toward NW and SE (red and green lines, respectively), as expected. This is also visible in the SGS images reported in Fig. 10b and c. When the wind blew toward the estuary, the plume was deviated toward SE (blue line), while the wind directed toward the sea deflected the plume toward NW (magenta line). This is because both the winds directed inside and outside the estuary had a component along the coastline. A correlation of the alongshore wind speed with the alongshore surface currents and the plume velocity immediately offshore of the river mouths was documented by Warrick et al. (2007), who found that the advection of plumes in the alongshore direction was dominated by local winds. Moreover, the larger was the alongshore component of the wind, the smaller was the plume offshore extension, because the plume was strongly and rapidly transported along the coast and did not expand toward the offshore. A similar result is reported by Osadchiev and Sedakov (2019), who studied the response of the Mzymta river plume to different forcing conditions. They showed that, for small rivers in microtidal environments, the near-field plume did not form a recirculating bulge adjacent to the river mouth, but directly transitioned to the wind-dominated far-field plume. Moreover, they observed that the offshore extension of the plume was smaller under a wind blowing in the alongshore direction. Such results were also in agreement with the findings of our PTV analysis (Section 3.2), which highlighted that the plume extension decreased with increasing alongshore velocity, mainly dominated by the wind force.

The effect of the wind associated with waves was shown in Fig. 11a and Fig. 11b, respectively for E and NNE waves. Blue and red lines refer to simulations run with no wind and wind concordant with the wave direction, while solid and dashed lines identify instants before and after the storm peak (t = 1 and t = 2). The plume bent either toward NW or SE under the action of wave-generated currents, as already seen in Section 4.1. Such currents developed in the alongshore direction just outside the river mouth and directly impacted on the plume evolution. Before the storm peak, when currents were not fully developed, the action of the wind caused the plume to strongly bend toward either NW or SE (red solid lines), reducing its offshore extension with respect to simulations with no wind (blue solid lines). Reaching the storm peak, the blue and red dashed lines got closer and closer, suggesting that the role of the wind in intensifying the effect of the wave-generated currents was no longer as effective.

4.3. Effect of the tide

The role of the tide in the plume generation and expansion was studied through two simulations where the 50 m^3/s discharge peak was taken to be simultaneous with high (ht) and low (lt) tide, respectively (Table 5). Fig. 12 shows that when the river discharge peak was coincident with the high tide (green line), the plume extension was lower than the case with no tide. This happened because the tidal current opposed the river current and increased the water depth, this reducing the flow velocity (Ruiz-Reina and López-Ruiz, 2021), the bed shear stress and consequently the suspended sediment concentration and the plume extension. Conversely, if the river discharge occurred concurrently with low tide (red line), the river flow velocity was enhanced, and the water depth decreased (Ruiz-Reina and López-Ruiz, 2021), this increasing the suspended concentration and the plume extension with respect to the simulation with no tide. In the simulated cases, we used the maximum tidal range for the MRE (0.6 m), which produced a change in the plume extension (compared with the RD 50 case) of about ± 9.5% in the RD 50 lt case and RD 50 ht case, respectively.

5. Conclusions

We studied the MR plume, reference for microtidal plumes, through the combined use of images, field data, numerical simulations and PTV analyses, allowing us to identify two local generation mechanisms (Section 4.1) and two main transport mechanisms (Section 4.2).

The most intense and extended plumes occurred during river discharge events due to both local resuspended sediment and material

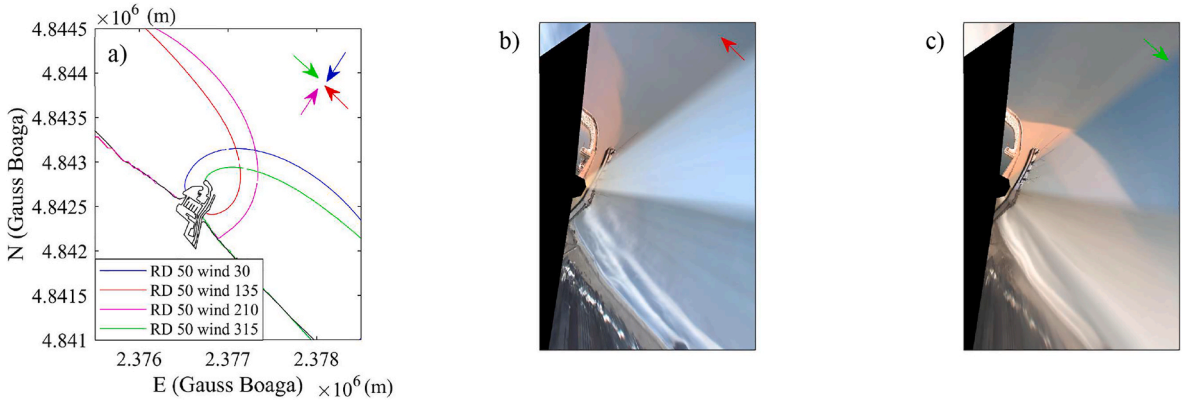

Fig. 10. a) Plume fronts resulting from the simulations forced with a river discharge peak of 50 m^3/s and different wind directions, also represented with coloured arrows; b) SGS image of a plume transported toward NW by south-easterly winds; c) SGS image of a plume transported toward SE by north-westerly winds.

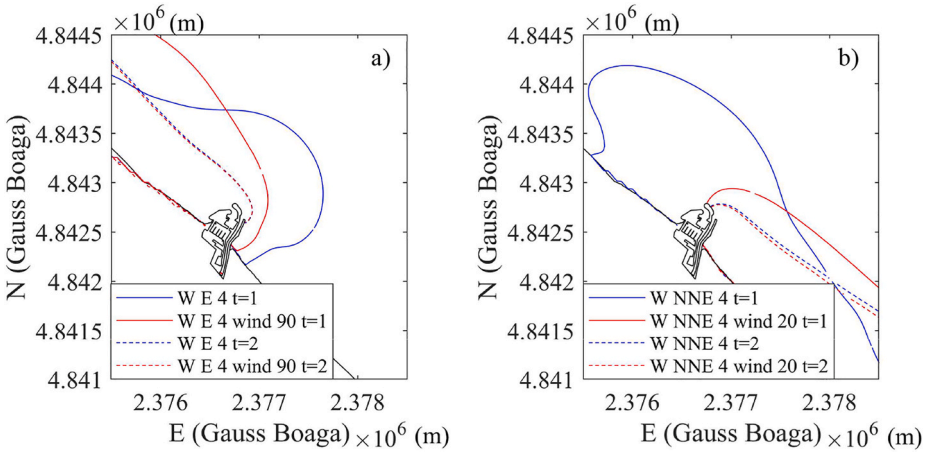

Fig. 11. Plume fronts resulting from the simulations run with a) E waves ($H_{s,max} = 4$m) and b) NNE waves ($H_{s,max} = 4$m), both alone (blue lines) and associated with a concordant wind (red lines). Solid and dashed lines refer to instants before and after the storm peak, respectively. (For interpretation of the references to colour in this figure legend, the reader is referred to the Web version of this article.)

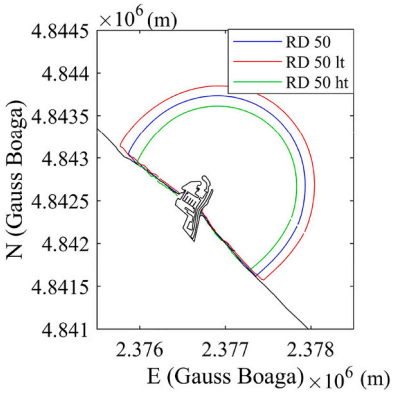

Fig. 12. Plume fronts for simulations forced with a river discharge peak of 50 m^3/s and no tide (blue line), high tide (green line) or low tide (red line) concomitant with the river discharge peak. (For interpretation of the references to colour in this figure legend, the reader is referred to the Web version of this article.)

supplied by the river flow from the upper part of the watershed (Figs. 6a and 9a).

Parametric simulations showed that river discharges that allowed to overcome the critical seabed shear stress threshold could resuspend the sediment and that the plume offshore extension and concentration increased with the river discharge (Fig. 9d). Supporting results came also by our PTV analyses, which showed that the river surface velocity increased with the river flow rate through a parabolic dependence (Fig. 7).

Plume events caused by waves were less dense than plumes generated by the river discharge. Real-life simulations highlighted that the concentration isoline followed by the observed plume front of the RD case (0.1 kg/m^3) was about twice the isoline corresponding to the front of the W case (0.059 kg/m^3). Furthermore, the parametric simulations confirmed that 5-year return period waves, resuspended less sediment than a river discharge associated to a return period smaller than 1 year. Our study highlights that, due to their important seabed stirring action, sea waves are a fundamental generation mechanism for plumes in microtidal environment, though the intensity of discharge-driven plumes is significantly larger than those driven by waves.

The wave action, opposing the river flow, kept the plume near the mouth. This was particularly evident for NNE waves that approached the coast nearly perpendicularly (Figs. 6b and 9c). Thus, the fate of the plume suspended sediment depended on the relative importance of river and wave forcings, as shown by Rodriguez et al. (2018) and Kastner et al. (2019). When wave momentum flux dominated, freshwater remained in the surf zone and mixed minimally, giving rise to well defined arched shapes (Fig. 9c). When river momentum flux dominated, most freshwater escaped the surf zone and was transported alongshore (Fig. 9a). Since the MR plume flows into an engineered channel that ends 300 m seaward from the shoreline, it is largely dominated by the bathymetry. For $H_s \leq 1.6$ m, waves break inshore of the ends of the jetties, this allowing the plume to escape the surf zone. Conversely, when $H_s \geq 2.4$ m, the width of the surf zone is larger than the length of the channel, trapping the plume inside the surf-zone under wave dominant conditions. Furthermore, oblique incoming waves deflected the plume along the coast, allowing the nourishment of farther beaches. Such alongshore transport was enhanced by the wind (Fig. 11a, b). Actually, the wind was the main transport mechanism and the major component of the alongshore plume surface velocity, contrasting the offshore spreading and mixing of freshwater discharge (Ostrander et al., 2008; Warrick et al., 2007): the larger was such alongshore velocity, the more the plume was pushed along the coast reducing its expansion toward the sea. Finally, we observed that the tide could affect the extension of the plume when the tidal excursion was set equal to the maximum tidal range for MRE (Fig. 12). However, in most common cases the tide could be neglected in comparison to the other mechanisms.

Fundamental result of our analysis is the relationship between the plume offshore extension and the ratio between the alongriver and alongshore plume velocities. This is given by a ¼ power law, as shown in Fig. 8d, which can be used as a simple proxy for the calculation of the plume extension.

Research data

The input file for the simulations, the observed dataset and the PTV data are available at the following Zenodo repository referenced in Baldoni et al. (2022).

CRediT authorship contribution statement

Agnese Baldoni: Writing – original draft, Visualization, Methodology, Investigation, Formal analysis, Data curation, Conceptualization. **Eleonora Perugini:** Writing – review & editing, Methodology, Formal analysis, Data curation, Conceptualization. **Pierluigi Penna:** Writing – review & editing, Resources, Data curation, Conceptualization. **Luca Parlagreco:** Writing – review & editing, Resources, Data curation,

Conceptualization. **Maurizio Brocchini:** Writing – review & editing, Supervision, Funding acquisition, Conceptualization.

Declaration of competing interest

The authors declare that they have no known competing financial interests or personal relationships that could have appeared to influence the work reported in this paper.

Data availability

I have shared the link to my dataset at the Attached File step.

Acknowledgments

The financial support from the Office of Naval Research Global (UK) MORSE Project (Research Grant N62909-17-1-2148) and from the Fondazione Cariverona 2019 PhD scholarship "Osservazione e MODellazione dell'idromorfoDINamica estuarina e costiera (OSMODIN)" (2019.0294 - D.R. n. 603 of May 28, 2019) is gratefully acknowledged. The authors would like to thank their colleagues who made significant contributions for both the field experiment and use of the SGS station, including Luciano Soldini, Joe Calantoni, Edward F. Braithwaite III, Alex Sheremet, Allen Reed, Margaret L. Palmsten. Additionally, the authors would like to thank the following authorities: the Municipality of Senigallia, the Capitaneria di Porto of Senigallia and of Ancona. Acknowledgments go also to: Civil Protection – Marche Region, Multi-risk Functional Center, GESTIPORT (Senigallia), Club Nautico (Senigallia), NOTA srl (Senigallia), Carmar Sub (Ancona), Sena Gallica (Senigallia), METIS S.R.L. (Senigallia).

Appendix A. Supplementary data

Supplementary data to this article can be found online at https://doi.org/10.1016/j.ecss.2022.107995.

References

Agnese Baldoni, Dataset, Perugini, Eleonora, Brocchini, Maurizio, Penna, Pierluigi, Parlagreco, Luca, 2022. In: Plume Data. https://doi.org/10.5281/zenodo.6795225.

AQUATER - REGIONE MARCHE, 1982. – Studio Generale per la difesa delle coste. In: Prima fase. Vol. II: rapporto di settore.

Asselman, N.E.M., 2000. Fitting and interpretation of sediment rating curves. J. Hydrol. 234 (3–4), 228–248. https://doi.org/10.1016/S0022-1694(00)00253-5.

Baldoni, A., Perugini, E., Soldini, L., Calantoni, J., Brocchini, M., 2021. Long-term evolution of an inner bar at the mouth of a microtidal river. Estuar. Coast Shelf Sci. https://doi.org/10.1016/j.ecss.2021.107573, 107573.

Bourrin, F., Friend, P.L., Amos, C.L., Manca, E., Ulses, C., Palanques, A., Durrieu de Madron, X., Thompson, C.E.L., 2008. Sediment dispersal from a typical Mediterranean flood: the Têt river, gulf of Lions. Continent. Shelf Res. 28 (15), 1895–1910. https://doi.org/10.1016/j.csr.2008.06.005.

Brando, V.E., Braga, F., Zaggia, L., Giardino, C., Bresciani, M., Matta, E., Bellafiore, D., Ferrarin, C., Maicu, F., Benetazzo, A., Bonaldo, D., Falcieri, F.M., Coluccelli, A., Russo, A., Carniel, S., 2015. High-resolution satellite turbidity and sea surface temperature observations of river plume interactions during a significant flood event. Ocean Sci. 11 (6), 909–920. https://doi.org/10.5194/os-11-909-2015.

Brocchini, M., Calantoni, J., Postacchini, M., Sheremet, A., Staples, T., Smith, J., Reed, A. H., BraithwaiteIII, E.F., Lorenzoni, C., Russo, A., Corvaro, S., Mancinelli, A., Soldini, L., 2017. Comparison between the wintertime and summertime dynamics of the Misa River estuary. Mar. Geol. 385, 27–40. https://doi.org/10.1016/j.margeo.2016.12.005.

Choi, B.J., Wilkin, J.L., 2007. The effect of wind on the dispersal of the Hudson River plume. J. Phys. Oceanogr. 37 (7), 1878–1897. https://doi.org/10.1175/JPO3081.1.

Cyriac, R., Dietrich, J.C., Blain, C.A., Dawson, C.N., Dresback, K.M., Fathi, A., Bilskie, M. V., Graber, H.C., Hagen, S.C., Kolar, R.L., 2020. Wind and tide effects on the Choctawhatchee Bay plume and implications for surface transport at Destin Inlet. Reg. Stud. Marine Sci. 35, 101131 https://doi.org/10.1016/j.rsma.2020.101131.

de Boer, G.J., Pietrzak, J.D., Winterwerp, J.C., 2009. SST observations of upwelling induced by tidal straining in the Rhine ROFI. Continent. Shelf Res. 29 (1), 263–277. https://doi.org/10.1016/j.csr.2007.06.011.

De Girolamo, A.M., Pappagallo, G., Porto, A.L., 2015. Temporal variability of suspended sediment transport and rating curves in a Mediterranean river basin: the Celone (SE Italy). Catena 128, 135–143. https://doi.org/10.1016/j.catena.2014.09.020.

Deltares, 2014. Delft3D-Flow, Simulation of multi-dimensional hydrodynamic flows and transport phenomena, including sediments. User Man. 684. Version 3.15.34158, May 2014.

Deltares, 2019. Delft3D-Wave, Simulation of short-crested waves with SWAN. User Man. (May 2019), 200. Version 3.05.58426.

Favali, P., Frugoni, F., Monna, D., Rainone, M.L., Signanini, P., Smriglio, G., 1995. The 1930 earthquake and the town of Senigallia (Central Italy): an approach to seismic risk evaluation. Ann. Geophys. 38 (5–6).

Fong, D.A., Geyer, W.R., 2001. Response of a river plume during an upwelling favorable wind event. J. Geophys. Res.: Oceans 106 (C1), 1067–1084. https://doi.org/10.1029/2000JC900134.

Frignani, M., Langone, L., Ravaioli, M., Sorgente, D., Alvisi, F., Albertazzi, S., 2005. Fine-sediment mass balance in the western Adriatic continental shelf over a century time scale. Mar. Geol. 222, 113–133. https://doi.org/10.1016/j.margeo.2005.06.016.

Garvine, R.W., 1995. A dynamical system for classifying buoyant coastal discharges. Continent. Shelf Res. 15 (13), 1585–1596. https://doi.org/10.1016/0278-4343(94)00065-U.

Harris, C.K., Sherwood, C.R., Signell, R.P., Bever, A.J., Warner, J.C., 2008. Sediment dispersal in the northwestern Adriatic Sea. J. Geophys. Res.: Oceans 113 (C11). https://doi.org/10.1029/2006JC003868.

Henderson-Sellers, B., 1988. The dependence of surface velocity in water bodies on wind velocity and latitude. Appl. Math. Model. 12 (2), 202–203. https://doi.org/10.1016/0307-904X(88)90012-1.

Janke, T., Schwarze, R., Bauer, K., 2020. Part2Track: a MATLAB package for double frame and time resolved Particle Tracking Velocimetry. SoftwareX 11, 100413. https://doi.org/10.1016/j.softx.2020.100413.

Janzen, C.D., Wong, K.C., 2002. Wind-forced dynamics at the estuary-shelf interface of a large coastal plain estuary. J. Geophys. Res.: Oceans 107 (C10). https://doi.org/10.1029/2001JC000959, 2-1.

Kastner, S.E., Horner-Devine, A.R., Thomson, J.M., 2019. A conceptual model of a river plume in the surf zone. J. Geophys. Res.: Oceans 124 (11), 8060–8078. https://doi.org/10.1029/2019JC015510.

Kombiadou, K., Krestenitis, Y.N., 2012. Fine sediment transport model for river influenced microtidal shelf seas with application to the Thermaikos Gulf (NW Aegean Sea). Continent. Shelf Res. 36, 41–62. https://doi.org/10.1016/j.csr.2012.01.009.

Korres, G., Ravdas, M., Zacharioudaki, A., 2019. Mediterranean Sea Waves Analysis and Forecast. CMEMS MED-Waves.

Lebedev, S.A., Kostianoy, A.G., Soloviev, D.M., Kostianaia, E.A., Ekba, Y.A., 2020. On a relationship between the river runoff and the river plume area in the northeastern Black Sea. Int. J. Rem. Sens. 41 (15), 5806–5818. https://doi.org/10.1080/01431161.2019.1685723.

Lee, H.J., Liu, K.K., 2013. Tidal effects on Changjiang plume dispersal in the East China sea. J. Mar. Sci. Technol. 21 (3), 342–352. https://doi.org/10.6119/JMST-013-0207-1.

Lesser, G., Roelvink, J., Van Kester, J., Stelling, G., 2004. Development and validation of a three-dimensional morphological model. Coastal Eng. 51, 883–915. https://doi.org/10.1016/j.coastaleng.2004.07.014.

Liu, Y., MacCready, P., Hickey, B.M., Dever, E.P., Kosro, P.M., Banas, N.S., 2009. Evaluation of a coastal ocean circulation model for the Columbia River plume in summer 2004. J. Geophys. Res.: Oceans 114 (C2). https://doi.org/10.1029/2008JC004929.

Melito, L., Postacchini, M., Sheremet, A., Calantoni, J., Zitti, G., Darvini, G., Penna, P., Brocchini, M., 2020. Hydrodynamics at a microtidal inlet: analysis of propagation of the main wave components. Estuar. Coast Shelf Sci. 235, 106603 https://doi.org/10.1016/j.ecss.2020.106603.

Mestres, M., Sierra, J.P., Sánchez-Arcilla, A., 2007. Factors influencing the spreading of a low-discharge river plume. Continent. Shelf Res. 27 (16), 2116–2134. https://doi.org/10.1016/j.csr.2007.05.008.

Milliman, J.D., Syvitski, J.P., 1992. Geomorphic/tectonic control of sediment discharge to the ocean: the importance of small mountainous rivers. J. Geol. 100 (5), 525–544. https://doi.org/10.1086/629606.

Mohamed, B., Abdallah, A.M., Alam El-Din, K., Nagy, H., Shaltout, M., 2019. Inter-annual variability and trends of sea level and sea surface temperature in the Mediterranean Sea over the last 25 years. Pure Appl. Geophys. 176 (8), 3787–3810. https://doi.org/10.1007/s00024-019-02156-w.

Morichon, D., Dailloux, D., Aarninkhof, S., Abadie, S., 2008. Using a shore-based video system to hourly monitor storm water plumes (Adour River, Bay of Biscay). J. Coast Res. (24), 133–140. https://doi.org/10.2112/06-0705.1.

Olabarrieta, M., Geyer, W.R., Kumar, N., 2014. The role of morphology and wave-current interaction at tidal inlets: an idealized modeling analysis. J. Geophys. Res.: Oceans 119 (12), 8818–8837. https://doi.org/10.1002/2014JC010191.

Osadchiev, A., Sedakov, R., 2019. Spreading dynamics of small river plumes off the northeastern coast of the Black Sea observed by Landsat 8 and Sentinel-2. Remote sensing of environment 221, 522–533. https://doi.org/10.1016/j.rse.2018.11.043.

Osadchiev, A., Zavialov, P., 2019. Structure and dynamics of plumes generated by small rivers. In: Estuaries and Coastal Zones-Dynamics and Response to Environmental Changes. IntechOpen.

Osadchiev, A., Barymova, A., Sedakov, R., Zhiba, R., Dbar, R., 2020. Spatial structure, short-temporal variability, and dynamical features of small river plumes as observed by aerial drones: case study of the Kodor and Bzyp river plumes. Rem. Sens. 12 (18), 3079. https://doi.org/10.3390/rs12183079.

Ostrander, C.E., McManus, M.A., Decarlo, E.H., Mackenzie, F.T., 2008. Temporal and spatial variability of freshwater plumes in a semi-enclosed estuarine–bay system. Estuar. Coast 31 (1), 192–203. https://doi.org/10.1007/s12237-007-9001-z.

Parlagreco, L., Melito, L., Devoti, S., Perugini, E., Soldini, L., Zitti, G., Brocchini, M., 2019. Monitoring for coastal resilience: preliminary data from five Italian sandy beaches. Sensors 19 (8), 1854. https://doi.org/10.3390/s19081854.

Perugini, E., Soldini, L., Palmsten, M., Calantoni, J., Brocchini, M., 2018. A new video monitoring station along the Adriatic Coast. XXXVI Convegno Nazionale di Idraulica e Costruzioni Idrauliche. IDRA2018, Ancona, Italy, pp. 12–14. September 2018.

Perugini, E., Soldini, L., Palmsten, M.L., Calantoni, J., Brocchini, M., 2019. Linear depth inversion sensitivity to wave viewing angle using synthetic optical video. Coastal Eng. 152 https://doi.org/10.1016/j.coastaleng.2019.103535.

Pigorini, B., 1968. Sources and dispersion of recent sediments of the Adriatic Sea. Mar. Geol. 6 (3), 187–229. https://doi.org/10.1016/0025-3227(68)90031-5.

Piñones, A., Valle-Levinson, A., Narváez, D.A., Vargas, C.A., Navarrete, S.A., Yuras, G., Castilla, J.C., 2005. Wind-induced diurnal variability in river plume motion. Estuar. Coast Shelf Sci. 65 (3), 513–525. https://doi.org/10.1016/j.ecss.2005.06.016.

Postacchini, M., Soldini, L., Lorenzoni, C., Mancinelli, A., 2017. Medium-term dynamics of a middle Adriatic barred beach. Ocean Sci. 13 (5), 719–734. https://doi.org/10.5194/os-13-719-2017, 2017.

Postacchini, M., Manning, A.J., Calantoni, J., Smith, J.P., Brocchini, M., 2022. A storm driven turbidity maximum in a microtidal estuary. Estuarine. Coastal and Shelf Science (under peer review).

Ravaioli, M., Bergami, C., Riminucci, F., Aracri, S., Aliani, S., Bastianini, M., Bergamasco, A., Bommarito, C., Borghini, M., Bozzano, R., Cantoni, C., Caterini, E., Cardin, V., Cesarini, C., Colucci, R.R., Crisafi, E., Crise, A., D'Adamo, R., Fanara, C., Giorgetti, A., Grilli, F., Langone, L., Lipizer, M., Marini, M., Menegon, S., Minuzzo, T., Miserocchi, S., Partescano, E., Paschini, E., Pavesi, F., Penna, P., Pensieri, S., Pugnetti, A., Raicich, F., di Sarra, A.G., Sarretta, A., Schroeder, K., Stanghellini, G., Vetrano, A., 2017. In: La rete scientifica italiana di siti fissi per l'osservazione del mare – IFON Stato dell'arte e upgrades durante il Progetto RITMARE (2012 – 2016). A cura di: Ravaioli M., Bergami C., Riminucci F.. CNR Pubblicazioni 2017, Roma, ISBN 978-88-80802-44-0, p. 50, 2017. (Accessed 2 April 2021).

REPORT - REGIONE MARCHE (2020).

Rodriguez, A.R., Giddings, S.N., Kumar, N., 2018. Impacts of nearshore wave-current interaction on transport and mixing of small-scale buoyant plumes. Geophys. Res. Lett. 45 (16), 8379–8389. https://doi.org/10.1029/2018GL078328.

Rolandi, G., Paone, A., Di Lascio, M., Stefani, G., 2008. The 79 AD eruption of Somma: the relationship between the date of the eruption and the southeast tephra dispersion. J. Volcanol. Geoth. Res. 169 (1–2), 87–98. https://doi.org/10.1016/j.jvolgeores.2007.08.020.

Ruiz-Reina, A., López-Ruiz, A., 2021. Short-term river mouth bar development during extreme river discharge events: the role of the phase difference between the peak discharge and the tidal level. Coastal Eng. https://doi.org/10.1016/j.coastaleng.2021.103982, 103982.

Simpson, J.H., Bos, W.G., Schirmer, F., Souza, A.J., Rippeth, T.P., Jones, S.E., Hydes, D., 1993. Periodic stratification in the Rhine ROFI in the north-sea. Oceanol. Acta 16 (1), 23–32. https://archimer.ifremer.fr/doc/00099/21050/.

Soosaar, E., Maljutenko, I., Uiboupin, R., Skudra, M., Raudsepp, U., 2016. River bulge evolution and dynamics in a non-tidal sea-Daugava River plume in the Gulf of Riga, Baltic Sea. Ocean Sci. 12 (2) https://doi.org/10.5194/os-12-417-2016.

Van Den Bremer, T.S., Breivik, Ø., 2018. Stokes drift. Phil. Trans. Math. Phys. Eng. Sci. 376 (2111), 20170104 https://doi.org/10.1098/rsta.2017.0104.

Warrick, J.A., DiGiacomo, P.M., Weisberg, S.B., Nezlin, N.P., Mengel, M., Jones, B.H., Ohlmann, J.C., Washburn, L., Terrill, E.J., Farnsworth, K.L., 2007. River plume patterns and dynamics within the Southern California Bight. Continent. Shelf Res. 27 (19), 2427–2448. https://doi.org/10.1016/j.csr.2007.06.015.

Whitney, M.M., Garvine, R.W., 2005. Wind influence on a coastal buoyant outflow. J. Geophys. Res.: Oceans 110 (C3). https://doi.org/10.1029/2003JC002261.

Yankovsky, A.E., Chapman, D.C., 1997. A simple theory for the fate of buoyant coastal discharges. J. Phys. Oceanogr. 27 (7), 1386–1401. https://journals.ametsoc.org/view/journals/phoc/27/7/1520-0485_1997_027_1386_astftf_2.0.co_2.xml.

Zarzuelo, C., López-Ruiz, A., Ortega-Sánchez, M., 2021. The role of waves and heat exchange in the hydrodynamics of multi-basin Bays: the example of Cádiz bay (southern Spain). J. Geophys. Res.: Oceans 126 (2), e2020JC016346. https://doi.org/10.1029/2020JC01634.